Digest Journal of Nanomaterials and Biostructures Vol. 20, No. 3, July - September 2025, p. 913 - 929

Enhanced energy storage performance of activated carbon through tannic acid-ferric ion coordination

C. Y. Chao [a], K. Y. Fu [a], R. Wang [b], Y. Jia [a], P. J. Li [a], H. Li [a,*]

[a] *Key Laboratory of Micro-Nano Materials for Energy Storage and Conversion of Henan Province, Institute of Surface Micro and Nano Materials, College of Chemical and Materials Engineering, Xuchang University, Henan 461000, P.R. China*

[b] *Tianjin Branch of China National Offshore Oil Corporation, Tianjin 300000, P.R. China*

This study modified activated carbon (AC) with tannic acid (TA) and ferric ions (Fe^{3+}) to create AC-TA-Fe composites for supercapacitor electrodes. AC-TA-$Fe_{0.2}$ showed the best performance, achieving a specific capacitance of 199.7 $F \cdot g^{-1}$ at 1 $A \cdot g^{-1}$. In a symmetric supercapacitor, it delivered 8.7 $Wh \cdot kg^{-1}$ at 2750 $W \cdot kg^{-1}$ and retained nearly 100% capacity after 10,000 cycles. The enhanced performance was due to the synergistic effects of TA and Fe, which improved surface redox activity, conductivity, and pore structure. This highlights TA and Fe-based modifications for efficient, durable electrode materials in energy storage.

(Received May 6, 2025; Accepted August 5, 2025)

Keywords: **S**upercapacitor, Phenol hydroxyl, Activated carbon, Electrochemical property, Cycle performance

1. Introduction

The rapid progress in the electronics industry, coupled with the increasing need for sustainable energy solutions, is driving the demand for more innovative energy conservation systems. Supercapacitors, as emerging energy storage systems, have garnered significant attention due to their exceptional power density, outstanding cycle stability, high safety, and environmental friendliness [1-6]. These features make them highly promising for applications in handheld devices, green energy solutions and other cutting-edge technologies. However, the widespread adoption of supercapacitors is still constrained by their relatively low energy density, which remains a critical challenge to overcome.

The electrochemical properties of supercapacitors are intrinsically linked to the structure of the electrode materials. Electrode materials made from carbon, especially activated carbon (AC), are extensively employed owing to their vast surface area, superior chemical stability, and environmental compatibility. Nevertheless, their specific capacitance is often considerably lower than that of pseudocapacitive-based materials, leading to energy density mismatch and limited

* Corresponding author: lihaoneu@xcu.edu.cn
https://doi.org/10.15251/DJNB.2025.203.913

overall performance [7-9]. To address this issue, there is an immediate necessity to develop advanced carbon-based materials with improved rate performance, definite capacitance and cycling resilience.

Recent research on AC-based materials has focused on optimizing porosity, incorporating functional groups, and doping with heteroatoms to enhance electrochemical performance [10-12]. For example, Lee et al. [13] demonstrated that functional group modification via nitric acid increased the specific capacitance of AC by approximately 160%. Deng et al. [14] utilized soybean dregs as the raw material, with phosphoric acid serving as both the activating agent and the phosphorus source, to synthesize nitrogen, oxygen, and phosphorus co-doped AC. The resulting heteroatoms co-doped AC featured a well-developed porous structure and revealed a specific capacity of 93.5 $F \cdot g^{-1}$ under a current density of 0.1 $A \cdot g^{-1}$ when tested in the aqueous electrolyte. Despite these achievements, a lot of existing strategies involve harsh preparation conditions, high costs, or environmental concerns, hindering their scalability and practicality for mass production.

Tannic acid (TA), a naturally abundant and inexpensive plant-derived polyphenol, has recently emerged as a promising material for modifying carbon-based electrodes. Its structure, characterized by a high density of phenol hydroxyl groups, provides unique chemical reactivity and redox activity [15, 16]. TA can be used to form stable coordination complexes with metal ions, such as Fe^{3+}, further amplifies its electrochemical activity and mechanical robustness [17, 18]. For instance, the interfacial coordination of TA with metal ions like Fe^{3+} facilitates the creation of metal-ligand structures on site, enhancing electrocatalytic activity [19]. Additionally, TA-based metal-phenolic networks have been explored for various bio-applications, highlighting their versatility [16]. In the realm of energy storage, mechanochemical coordination of TA and Fe^{3+} has been employed to fabricate highly microporous carbon materials, demonstrating significant potential as advanced supercapacitor electrodes [5]. These studies underscore the promise of TA and Fe^{3+} coordination complexes in developing high efficiency materials for supercapacitors.

In this study, we propose a novel method for modifying AC by utilizing TA and Fe^{3+} to form AC-TA-Fe composites via coordination reactions. The incorporation of TA and Fe^{3+} is expected to provide more redox-active locations and enhance the conductivity and surface properties of AC, thereby significantly enhancing its specific capacitance and rate performance. This work aims to overcome the limitations of conventional AC materials and offer a fresh perspective for designing superior carbon-derived materials for supercapacitors.

2. Experimental

2.1. Materials

The following materials were used in the experiments: AC, TA, $FeCl_3 \cdot 6H_2O$, NaOH, HCl and polyvinylidene fluoride (PVDF). All chemicals were of analytical grade and were applied as they were received, without any additional purification.

2.2. Preparation of modified electrode materials

2.2.1. Synthesis of AC-TA-Fe composites

To synthesize the AC-TA-Fe composites, 0.5 g of AC and 5 g of TA were dissolved in 200 mL of deionized water, followed by sonication for 30 minutes to ensure uniform dispersion. Subsequently, a specified amount of $FeCl_3 \cdot 6H_2O$ (determined based on mass ratios of AC:TA:Fe as 1:10:x, where *x* denotes the Fe proportion) was added to the mixture after dissolving in 20 mL of deionized water. A 0.1 $mol \cdot L^{-1}$ NaOH solution was used to adjust the pH of the solution to between 7 and 8, and the mixture was left undisturbed for 2 hours. The precipitated solids were then divided by centrifugation, rinsed thoroughly with deionized water, and dried at 80°C. The final products were designated as AC-TA-Fe(*x*), where *x* represents the Fe proportion.

2.2.2. Preparation of working electrodes

AC-TA-Fe, acetylene black, and PVDF were combined in a weight proportion of 7:2:1 by weight. The mixture was homogenized with 2 mL of NMP under continuous grinding and sonicated for 30 minutes to form a viscous slurry. Approximately 110 μL of the prepared slurry was cast onto a 1 × 1 cm region of the nickel foam substrate. The coated electrodes were placed in an oven and dried at 100°C for 2 hours and subsequently pressed at 10 MPa for 1 minute to improve the adhesion and compactness of the active material. The active material loading was determined by measuring the mass difference of the nickel foam before and after coating. In this work, the active material was loaded with a mass ranging from 3 to 4 $mg \cdot cm^{-2}$.

2.3. Characterization and electrochemical measurements

2.3.1. Physical characterization

The morphology was examined by SEM (S-4800, Hitachi, Tokyo, Japan), coupled with EDS for elemental mapping to assess the distribution of key elements across the samples. The crystallographic structure was examined using X-ray diffractometer (XRD, Bruker D8) with Cu Kα radiation (λ = 1.54 Å) at a resolution of 0.82 Å. The FTIR spectra were tested on a Bruker Tensor 27 spectrometer to investigate functional group variations. Thermogravimetric analysis (TGA) was studied on the Netzsch STA2500 thermal analyzer under N_2 atmosphere in the range of 30-600°C to evaluate thermal stability. The specific surface area and pore structure were assessed using adsorption-desorption curves obtained from a Micromeritics ASAP 2460 instrument. The surface elemental state and chemical configurations was analyzed by XPS measurement.

2.3.2. Electrochemical testing in a three-electrode system

The tests were arranged with a three-electrode setup, using the as-prepared electrodes served as the working electrode, Hg/HgO as reference electrode and Pt as the counter electrode in the KOH solution (6 M). Electrochemical characterization was tested using a PGSTAT302N workstation for CV, GCD and EIS analysis. Cycle stability were characterized on Neware BTS electrochemical analyzers. The GCD data was used to calculate the specific capacitance using the following formula:

$$C = \frac{I\Delta t}{m\Delta V} \tag{1}$$

In this context, I stands for the discharge current (A), ΔV signifies the potential

window (V), Δt represents the discharge time in seconds, and m indicates the mass of the active material (g).

2.3.3. Symmetric supercapacitor testing

Symmetric supercapacitors were assembled using two identical electrodes with approximately equal active material loading. The electrolyte and procedures for testing were the same as in the three-electrode system. Energy density (E, $Wh \cdot kg^{-1}$) and power density (P, $kW \cdot kg^{-1}$) were calculated using the equations:

$$E = \frac{C_{cell}\Delta V^2}{7.2} \tag{2}$$

$$P = \frac{3.6E}{t} \tag{3}$$

where ΔV and t have the same physical significance as in Equation 1, and C_{cell} is the specific capacitance of the device.

3. Results and discussion

The morphology and elemental distribution of the raw materials and modified composites are presented (Figure 1). TA appears as smooth spherical particles (Figure 1a), while AC exhibits irregular blocky morphology, reflecting its porous characteristics and complex surface structure (Figure 1b). The modified samples, AC-TA-$Fe_{0.1\text{-}0.5}$, retain the overall morphology of AC (Figure 1c-e), indicating that TA and Fe are uniformly dispersed on the surface through chemical reactions without significant phase separation. However, as the Fe content increases further (Figure 1f), TA-Fe complexes begin to form isolated particles, likely due to local precipitation and reduced dispersibility caused by high Fe concentration.

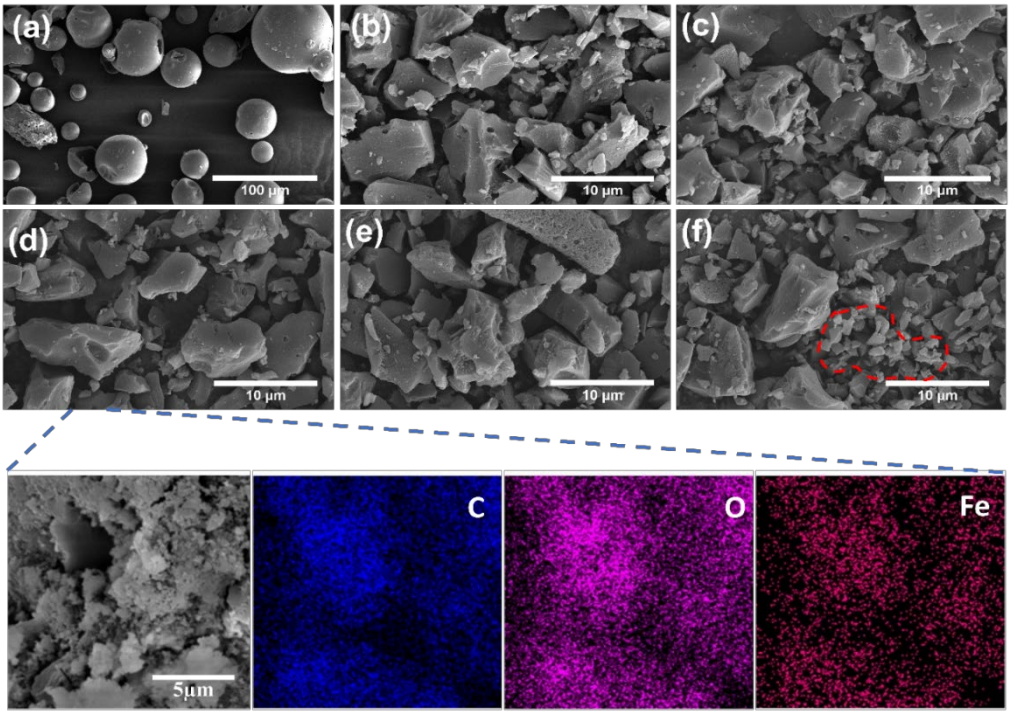

Fig. 1. SEM images of (a)TA, (b)AC, (c)AC-TA-$Fe_{0.1}$, (d)AC-TA-$Fe_{0.2}$, (e)AC-TA-$Fe_{0.5}$, (f)AC-TA-Fe_1 and EDS of AC-TA-$Fe_{0.2}$ sample.

The EDS result reveals that the AC-TA-$Fe_{0.2}$ sample is primarily composed of C, O and Fe, with Fe uniformly distributed, demonstrating that TA-Fe complexes are successfully and evenly anchored on the AC surface. This uniform distribution prevents phase separation while providing additional electrochemical active sites, which enhance the energy storage capabilities and electrochemical stability of the material. The particle aggregation observed at higher Fe concentrations necessitates further optimization of the synthesis conditions.

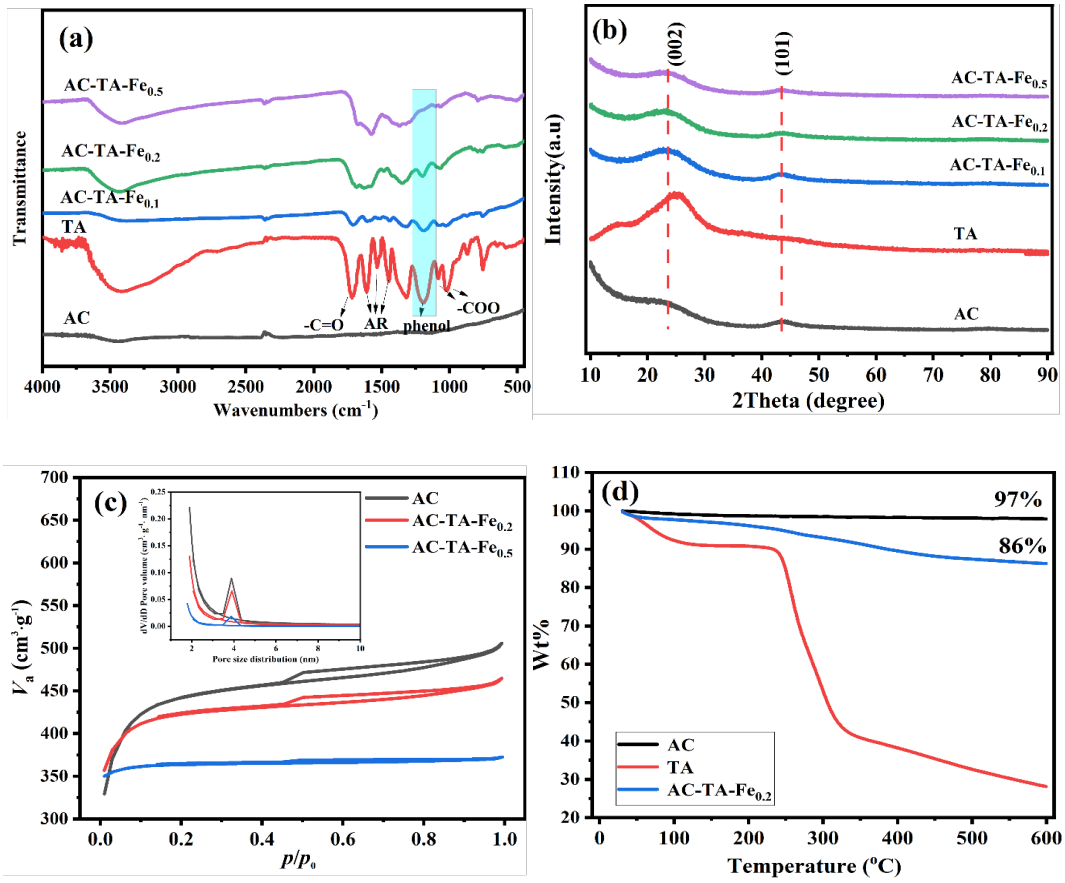

Fig. 2. (a) FTIR spectra, (b)XRD patterns, (c) N_2 adsorption-desorption isotherms and (d)TGA curves of as prepared samples.

The FTIR spectra of AC, TA and the modified samples are provided to analyze changes in surface functional groups (Figure 2a). The AC spectrum shows a weak O-H absorption band at 3500 cm^{-1}, indicating a small amount of adsorbed water, with few distinct peaks representing functional groups. This suggests low surface chemical activity. In contrast, the TA spectrum exhibits multiple prominent peaks, including a wide absorption band at 3500-3200 cm^{-1} corresponding to O-H bond stretching, a sharp peak associated with C=O stretching at 1715 cm^{-1}, and aromatic ring vibrations in the range of 1450-1600 cm^{-1} [20, 21]. This points to a large number of functional groups being present in TA, which serve as active sites for subsequent coordination with Fe. In the modified samples, the phenol absorption peak at 1196 cm^{-1} diminishes in intensity with increasing Fe content, indicating the coordination formed

between Fe ions and the phenolic hydroxyl groups in TA [22, 23]. These changes enhance the surface activity of the materials, making them more suitable for electrochemical applications in energy storage devices.

The XRD patterns of AC, TA and the modified samples are shown to evaluate their crystal structure and degree of crystallinity (Figure 2b). AC displays broad peaks at 23° and 43°, corresponding to the (002) and (101) planes, respectively, characteristic of amorphous carbon with low graphitization [10, 24]. TA exhibits a broad peak at approximately 25°, indicating partial crystallinity in its organic molecular structure. After modification with TA and Fe, the composite retains the characteristic peaks of graphitized carbon, while the distinct TA peaks disappear, signifying the uniform dispersion of TA within the composite without forming separate crystalline phases. This structural adjustment alters the microstructure without affecting the amorphous nature of AC. Such modifications may enhance the conductivity and ion transport properties of the composites, increasing their suitability for applications in energy storage.

The N_2 adsorption-desorption curves for AC and the modified samples are presented (Figure 2c). All samples exhibit type IV isotherms, indicative of materials containing micropores and mesopores [25, 26]. AC demonstrates a high adsorption capacity of 489 $cm^3 \cdot g^{-1}$ at a relative pressure of $p/p_0 = 0.9$, reflecting a well-developed pore structure and a large specific surface area. In contrast, the adsorption capacities of the modified samples decrease significantly, with values of 452 $cm^3 \cdot g^{-1}$ and 368 $cm^3 \cdot g^{-1}$ for AC-TA-$Fe_{0.2}$ and AC-TA-$Fe_{0.5}$, respectively, indicating a reduction in specific surface area due to the modification process. The pore size distribution shows that the primary pore size of AC is around 2 nm, and while the modified samples retain a similar pore size peak, the distribution shifts slightly toward the 3-4 nm range. This suggests that the introduction of TA and Fe primarily modifies the pore walls chemically rather than restructuring the architecture of the corresponding material. Despite the reduction in specific surface area and adsorption capacity, the slight expansion toward the mesoporous range improves ion diffusion and electrolyte wettability, which are vital for improving the electrochemical performance of supercapacitors and other energy storage devices.

The TGA curves for AC, TA, and the modified samples are shown to evaluate thermal stability (Figure 2d). AC exhibits excellent thermal stability, losing approximately 3% of its mass below 100°C due to water evaporation and retaining 97% of its mass at higher temperatures [27]. In comparison, TA undergoes significant decomposition between 100°C and 350°C, with the initial loss attributed to the evaporation of water associated with phenolic hydroxyl groups, and further decomposition of its organic molecular framework occurring between 200°C and 350°C. By 600°C, TA retains only about 30% of its initial mass [28, 29]. The AC-TA-$Fe_{0.2}$ sample shows intermediate thermal stability, losing approximately 14% of its mass between 300°C and 500°C, with a final retention of 86%. Although the introduction of TA reduces thermal stability, the relatively low TA content ensures that the material's structural integrity is preserved, meeting the thermal stability requirements of practical energy storage applications.

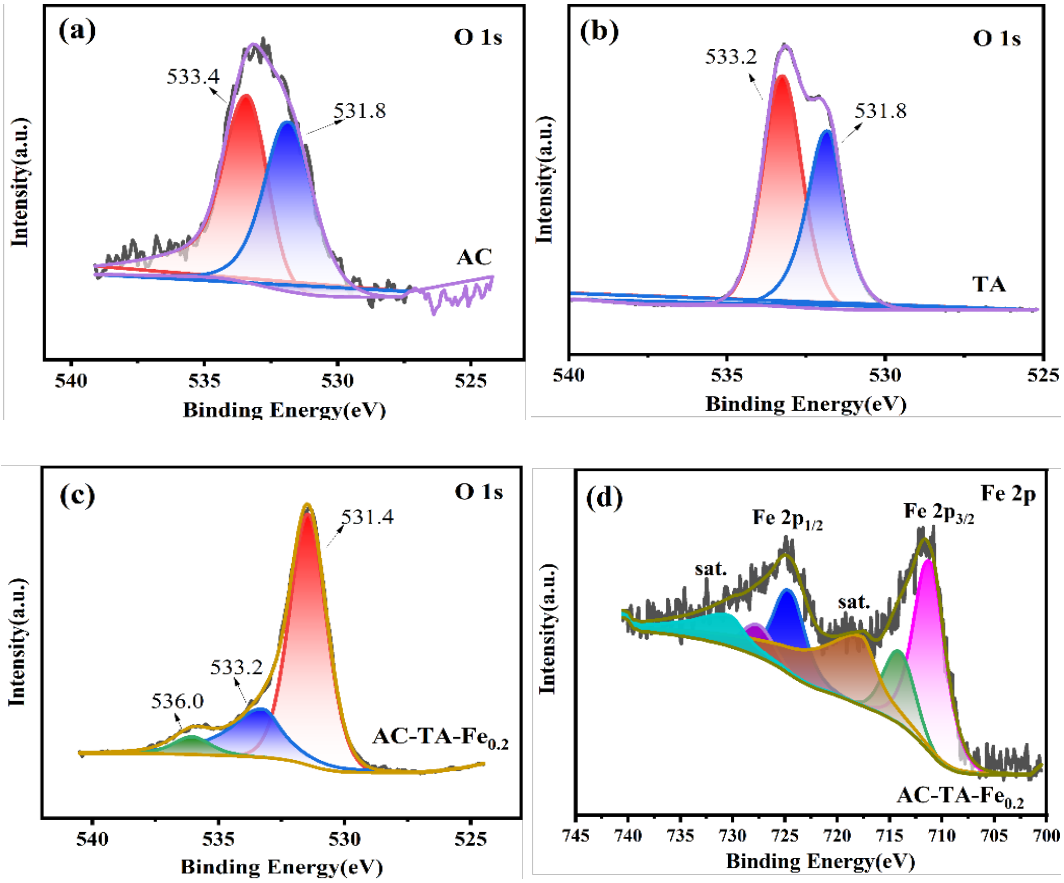

Fig. 3. (a-c) O 1s spectra of AC, TA and AC-TA-Fe$_{0.2}$ samples; (d) Fe 2p spectra of AC-TA-Fe$_{0.2}$.

The XPS analysis reveals significant differences in the surface chemical environments of AC, TA and AC-TA-Fe$_{0.2}$ samples (Figure 3). In the O 1s spectrum, the AC sample shows a weak peak at approximately 531.5 eV, corresponding primarily to a small amount of surface carbonyl groups (C=O), indicating a low content of functional groups that contain oxygen [30]. On the other hand, the TA sample exhibits prominent peaks at 531.8 eV (C=O) and 533.2 eV (phenolic hydroxyl groups, C-OH), reflecting its rich phenolic and carbonyl structures [20, 31]. In the modified AC-TA-Fe$_{0.2}$ sample, the intensity of the phenolic hydroxyl peak at 533.2 eV decreases significantly, indicating that some phenolic hydroxyl groups have formed stable C-O-Fe bonds through coordination with Fe^{3+} [32]. Although no distinct Fe-O peaks are observed, the coordination of Fe^{3+} is indirectly evidenced by the transformation of phenolic hydroxyl groups.

The Fe 2p spectrum of AC-TA-Fe$_{0.2}$ further confirms the occurrence of coordination interactions. The spectrum displays characteristic Fe^{3+} peaks, including the primary Fe 2p$_{3/2}$ peak at approximately 711.1 eV and Fe 2p$_{1/2}$ peak near 724.5 eV, indicative of the presence of Fe^{3+} in the sample. Additionally, peaks at 714.1 eV and 727.5 eV are attributed to vibrational satellite peaks arising from interactions between Fe^{3+} and ligands, suggesting the formation of a stable coordination state. The satellite peaks at 717.6 eV and 730.3 eV, characteristic of Fe^{3+}, further confirm the high-valence state of iron within the material [32]. The high proportion of Fe^{3+} and its coordination structure introduce additional areas for redox processes, significantly enhancing the pseudocapacitive performance of the sample.

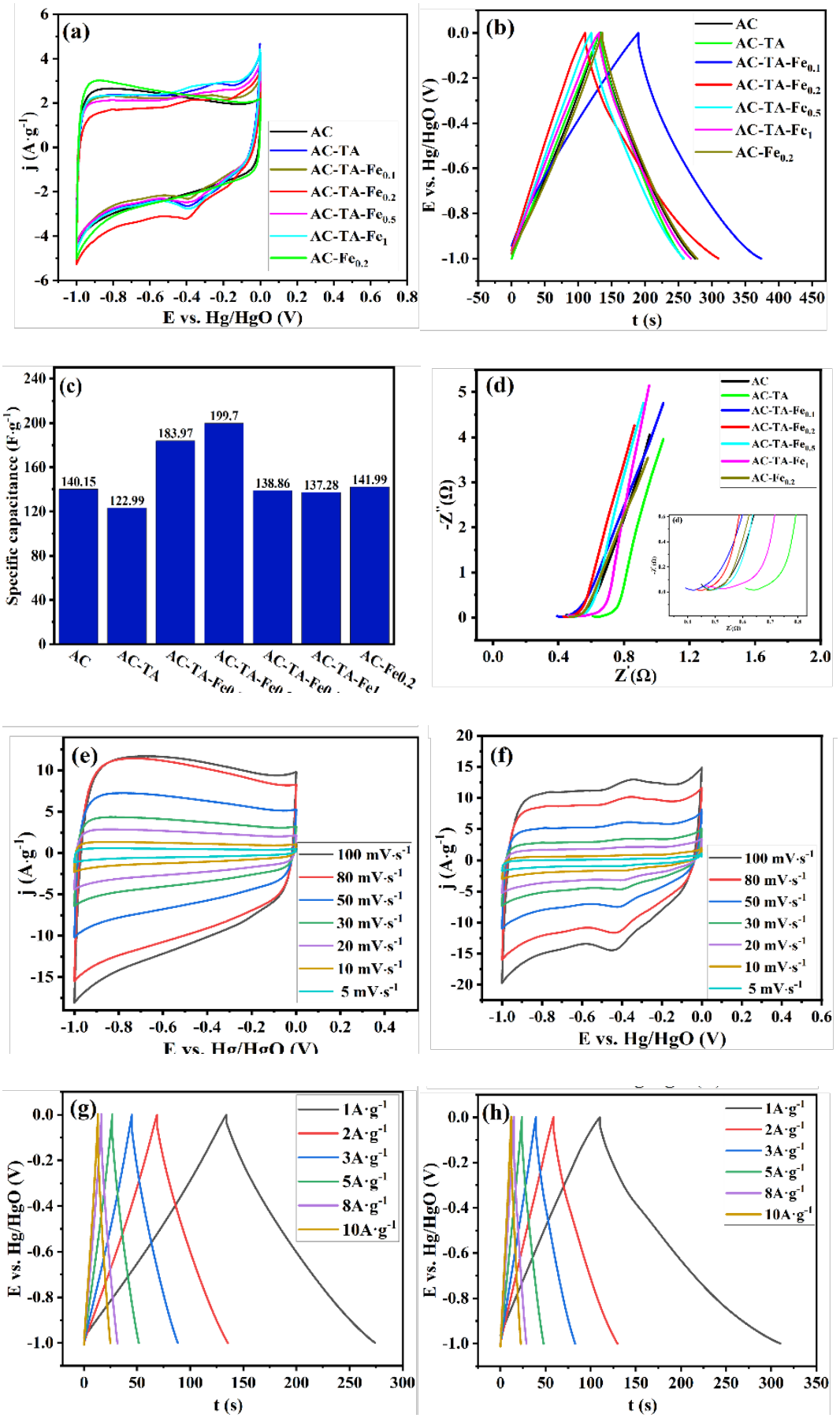
(a)
j (A·g⁻¹)
E vs. Hg/HgO (V)
AC
AC-TA
AC-TA-Fe0.1
AC-TA-Fe0.2
AC-TA-Fe0.5
AC-TA-Fe1
AC-Fe0.2
(b)
E vs. Hg/HgO (V)
t (s)
(c)
Specific capacitance (F·g⁻¹)
140.15
122.99
183.97
199.7
138.86
137.28
141.99
AC
AC-TA
AC-TA-Fe0.1
AC-TA-Fe0.2
AC-TA-Fe0.5
AC-TA-Fe1
AC-Fe0.2
(d)
-Z''(Ω)
Z'(Ω)
(e)
j (A·g⁻¹)
100 mV·s⁻¹
80 mV·s⁻¹
50 mV·s⁻¹
30 mV·s⁻¹
20 mV·s⁻¹
10 mV·s⁻¹
5 mV·s⁻¹
E vs. Hg/HgO (V)
(f)
j (A·g⁻¹)
E vs. Hg/HgO (V)
(g)
E vs. Hg/HgO (V)
1A·g⁻¹
2A·g⁻¹
3A·g⁻¹
5A·g⁻¹
8A·g⁻¹
10A·g⁻¹
t (s)
(h)
E vs. Hg/HgO (V)
t (s)

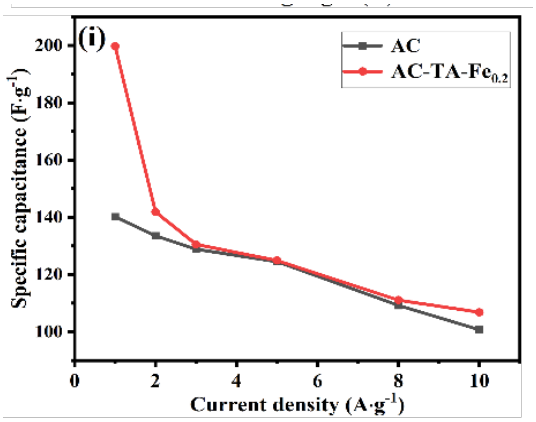

Fig. 4. (a) CV profiles at 20 mV·s^{-1}, (b) GCD profiles at 1 A·g^{-1}, (c) specific capacity and (d) EIS of electrodes; CV curves at various scan rates for (e) AC and (f) AC-TA-Fe$_{0.2}$ electrodes, GCD profiles at various current densities for (g) AC and (h) AC-TA-Fe$_{0.2}$ electrodes; (i) specific capacitance comparison for AC and AC-TA-Fe$_{0.2}$ electrodes.

The CV results for AC and its modified samples at the 20 mV·s^{-1} scan rate are displayed, showing a significant enhancement in electrochemical performance after modification (Figure 4a). The CV curve of unmodified AC is nearly rectangular, indicating that its energy storage mechanism primarily relies on EDLC process, where ions undergo rapid physical adsorption at the interface between electrolyte and electrode materials [26, 33]. In comparison, the CV areas of AC-TA and AC-TA-Fe samples increase markedly, with redox peaks appearing in the -0.2 to -0.4 V range, indicating the presence of pseudocapacitive effects. These advancements are a result of introducing TA and Fe, which increase electrochemical active sites and facilitate Faradaic redox reactions. Among the samples, AC-TA-Fe$_{0.2}$ exhibits the largest CV area, reflecting the most optimal electrochemical performance and highlighting the synergistic effects of TA-Fe modifications in improving energy storage capabilities. The pseudocapacitance contribution from TA and its Fe complexes involves two mechanisms [34, 35]:

- Redox reactions of phenolic hydroxyl groups

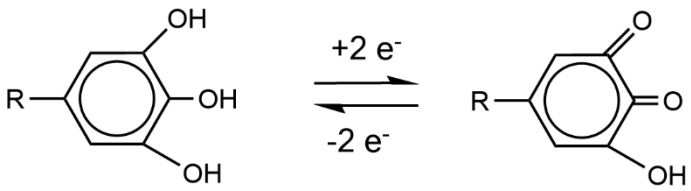

- Redox cycling between Fe^{3+} and Fe^{2+}

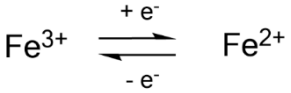

The GCD curves at 1 $A \cdot g^{-1}$ further demonstrate the specific capacitance performance of the samples (Figure 4b). The unmodified AC exhibits an isosceles triangular profile, characteristic of EDLC mechanisms, with minimal voltage hysteresis, indicating good coulombic efficiency. In contrast, the modified samples show enhanced non-linear features in their GCD curves, corresponding to pseudocapacitive effects [36]. The discharge time is significantly extended, especially for AC-TA-$Fe_{0.2}$, which achieves the longest discharge duration, demonstrating superior energy storage performance. This improvement stems from the synergistic effects of TA and Fe, which not only enhance surface redox activity but also optimize conductivity and pore structure.

The specific capacitance variations among the samples are quantified in bar graphs (Figure 4c). The unmodified AC exhibits a specific capacitance of 140.15 $F \cdot g^{-1}$. Interestingly, TA modification slightly reduces the capacitance to 122.99 $F \cdot g^{-1}$, likely due to the partial deactivation of micropores caused by the introduction of TA, which decreases the EDLC contribution. However, with the incorporation of Fe, the specific capacitance increases significantly, reaching 199.7 $F \cdot g^{-1}$ for AC-TA-$Fe_{0.2}$, the highest among all samples. This indicates that an optimal Fe content substantially enhances energy storage performance by leveraging redox activity while maintaining good electrolyte wettability and ion transport.

The EIS plots highlight the electrochemical dynamics of the samples (Figure 4d). The modified samples exhibit a noticeable reduction in impedance. The semi-circle in the high-frequency zone corresponding to charge transfer resistance (R_{ct}) is not prominent, which is attributed to the good conductivity of the carbon materials, resulting in a relatively low resistance at the junction of the electrode and electrolyte. Within the low-frequency zone, the warburg slope of AC-TA-$Fe_{0.2}$ approaches vertical, signifying superior ion diffusion and faster charge transfer [32, 37]. By comparison, the unmodified AC sample exhibits significantly higher impedance, demonstrating the effectiveness of the modification in enhancing the electrochemical dynamics. Overall, AC-TA-$Fe_{0.2}$ performs best in terms of conductivity and ion transport, and these factors are vital for reaching high-power efficiency in supercapacitors.

The CV curves of AC (Figure 4e) show minimal area growth compared to the modified samples at different scan rates, with no evident pseudocapacitive features. With increasing the scan rate, the rectangular shape begins to distort, indicating that its energy storage relies entirely on EDLC mechanisms. The lack of pseudocapacitive active sites limits its performance, especially at high scan rates where ion diffusion and charge transfer become constrained [38]. In contrast, the CV curves of AC-TA-$Fe_{0.2}$ at varying scan rates (Figure 4f) demonstrate excellent electrochemical stability and rapid kinetic properties. With alterations in the scan rate ranging from 5 to 100 $mV \cdot s^{-1}$, the CV area grows progressively while maintaining symmetry, and the redox peaks remain clearly visible. This indicates efficient charge transport and stable pseudocapacitive behavior, even at high scan rates, making AC-TA-$Fe_{0.2}$ suitable for high-power-density applications, where it can respond quickly to current variations without significant loss of storage capacity.

The GCD profiles for AC reveal a significant decline in rate performance (Figure 4g). As the current density increases from 1 to 10 $A \cdot g^{-1}$, the discharge time decreases drastically, reflecting limited ion diffusion and charge transport under high-current conditions. The increased slope at higher current densities indicates rising internal resistance, resulting in lower coulombic efficiency and restricted high-power applications for AC [13]. Conversely, the GCD curves for

AC-TA-$Fe_{0.2}$ at different current densities demonstrate superior rate performance (Figure 4h). Even at 10 $A \cdot g^{-1}$, the discharge time remains relatively long, indicating low internal resistance and efficient charge transport. The performance enhancement can be attributed to uniformly distributed Fe active sites and an optimized pore structure, which collectively increase charge storage capacity and improve ion diffusion efficiency.

The specific capacitance trends of AC and AC-TA-$Fe_{0.2}$ at different current densities are summarized (Figure 4i). At low current densities (1 $A \cdot g^{-1}$), AC-TA-$Fe_{0.2}$ achieves a specific capacitance of approximately 200 $F \cdot g^{-1}$, significantly higher than the 140 $F \cdot g^{-1}$ of AC, showing its clear advantage. When current densities are higher, the capacitance difference between the two samples narrows but remains noticeable. The performance improvement arises from the synergistic effects of TA and Fe modification: first, the redox-active sites generated by the coordination between phenolic hydroxyl groups and Fe enhance pseudocapacitance; second, the pore size distribution shifts towards the mesoporous range, as shown by BET analysis, improving electrolyte wettability and ion transport; finally, the uniform distribution of Fe increases conductivity and reduces interfacial resistance [17, 39].

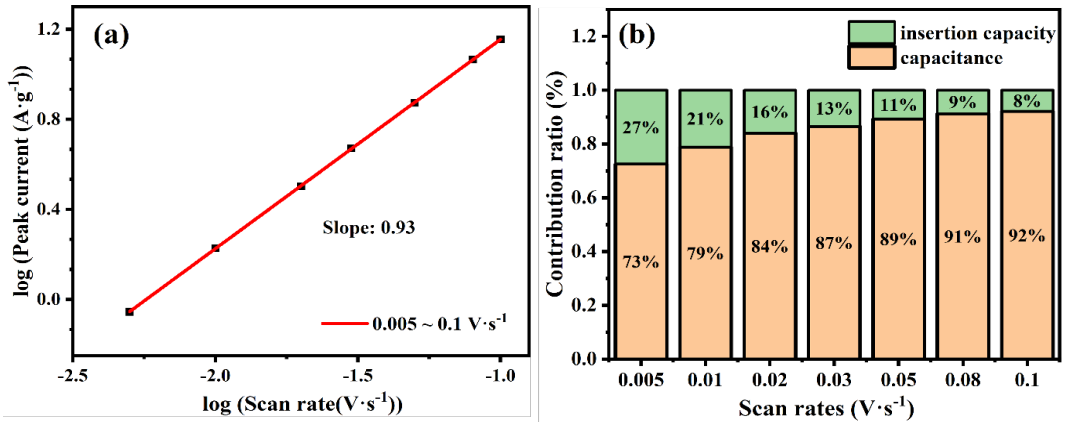

Fig. 5. (a) Fitting curve of the cathodic peak currents, (b) different ratio of the capacity versus scan rate for AC-TA-$Fe_{0.2}$ electrode.

To gain a more profound comprehension of the electrochemical mechanism of the AC-TA-$Fe_{0.2}$ electrode, a kinetic analysis of CV data was conducted. The scan rate (v) and corresponding peak current (i) was fitted using the $i = a\ v^b$ formula and the separation formula i (V) = $k_1 v + k_2 v^{1/2}$, allowing quantitative evaluation of the contributions from pseudocapacitance and EDLC to the total current [40, 41].

The linear fitting of the log-log plot of i versus v over the range of 0.005-0.1 $V \cdot s^{-1}$ yields a slope (b) of 0.93 (Figure 5a). This value suggests that the energy storage mechanism of the AC-TA-$Fe_{0.2}$ electrode is predominantly surface capacitance behavior ($b \approx 1$). It indicates that the storage process is dominated by EDLC and rapid surface Faradaic reactions, where ion adsorption and redox reactions occur swiftly at the surface of the electrode. The b value approaching 1 further implies that the electrode exhibits excellent charge transport and energy storage capabilities even at high scan rates [42, 43].

The impact of EDLC (orange zone) and pseudocapacitance (green zone) at various scan rates is illustrated (Figure 5b). At 0.005 $V \cdot s^{-1}$ scan rate, pseudocapacitance accounts for 27% of the total current, while EDLC contributes 73%. This indicates that ions have enough time to diffuse into the pores or reach active sites within the material at lower scan rates, leading to diffusion-limited Faradaic reactions with a higher pseudocapacitive contribution. However, the pseudocapacitive contribution gradually decreases to 8% at 0.1 $V \cdot s^{-1}$, while the EDLC contribution rises to 92% with the scan rate increases. This shift occurs because, at higher scan rates, the diffusion-limited pseudocapacitive mechanism is suppressed, and the surface-dominated EDLC effect, characterized by rapid ion adsorption and desorption, becomes dominant [44, 45].

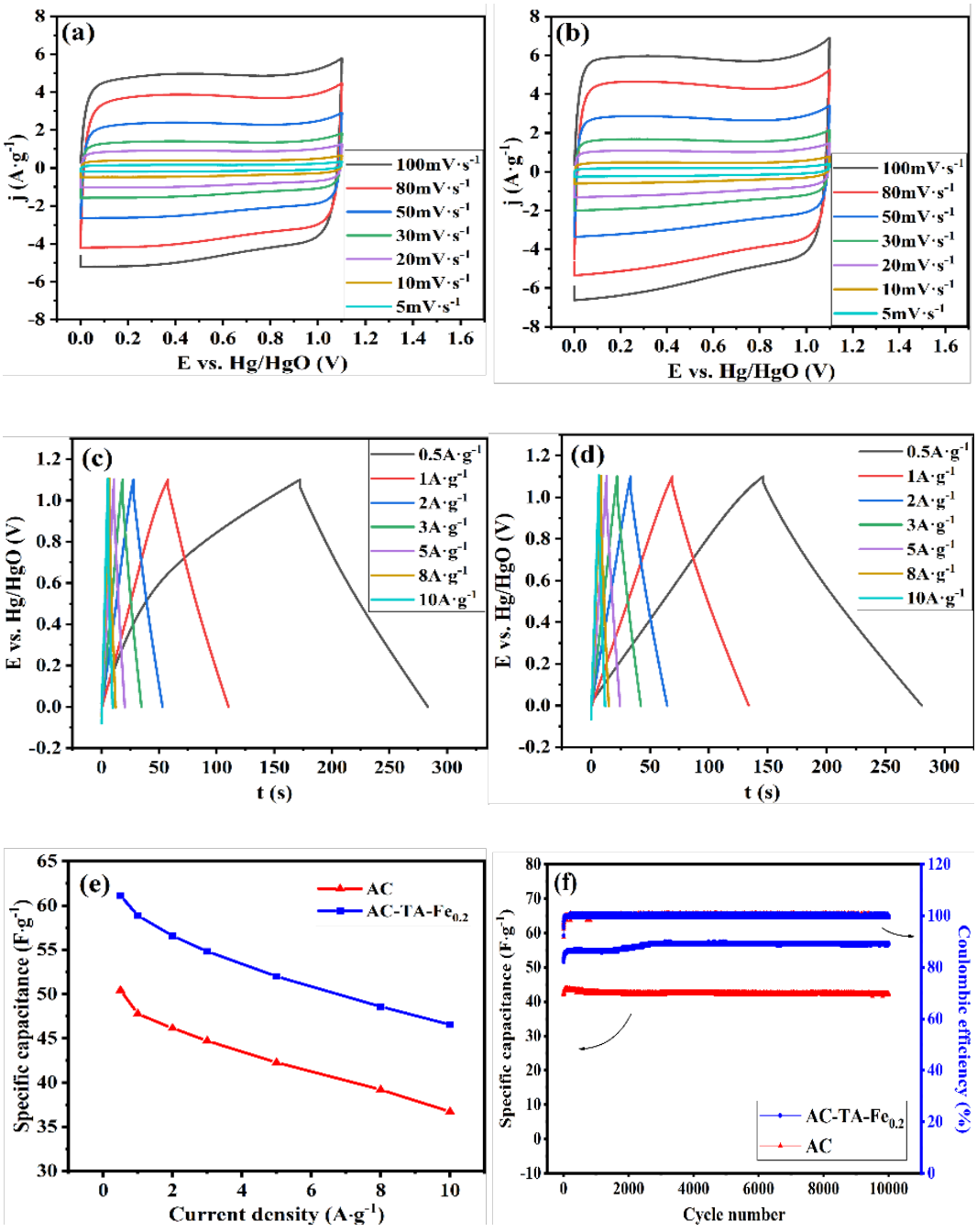

Fig. 6. Symmetric supercapacitor performance: CV profiles at different scan rates for (a) AC and (b) AC-TA-$Fe_{0.2}$, GCD profiles for (c) AC and (d) AC-TA-$Fe_{0.2}$ electrodes; (e) comparison of capacitance and long-term cycle stability (5 $A \cdot g^{-1}$).

This trend highlights the dynamic energy storage mechanism transition of the AC-TA-$Fe_{0.2}$ electrode under different operational conditions. At low scan rates, pseudocapacitance and EDLC synergistically contribute to energy storage. At high scan rates, the fast EDLC effect becomes the primary mechanism, demonstrating its adaptability and high performance under varying conditions.

To further evaluate the differences in energy storage performance between AC and AC-TA-$Fe_{0.2}$ in practical applications, symmetric supercapacitors were assembled using each as the electrode material. Their performance was characterized through CV, GCD, rate and cycling performance tests. The CV profiles (5-100 $mV \cdot s^{-1}$) for the symmetric supercapacitors are shown in Figure 6a-b. The CV of AC-based supercapacitor displays a nearly rectangular shape, indicating its energy storage mechanism primarily relies on EDLC. In contrast, the AC-TA-$Fe_{0.2}$ based supercapacitor demonstrates a significantly larger CV area, with small redox peaks appearing at low scan rates (e.g., 5 $mV \cdot s^{-1}$), highlighting the contribution of pseudocapacitive effects. This suggests that AC-TA-$Fe_{0.2}$ not only retains excellent EDLC properties but also enhances energy storage capacity through surface redox reactions.

The GCD behavior at various current densities for the two supercapacitors is shown in Figure 6c-d. In the AC based supercapacitor, the current-voltage curves appear as symmetric triangles, indicating good coulombic efficiency. However, the AC-TA-$Fe_{0.2}$ based supercapacitor shows significantly longer discharge times, particularly at low current density (0.5 $A \cdot g^{-1}$), reflecting higher specific capacitance. Additionally, the AC-TA-$Fe_{0.2}$ charge-discharge curves exhibit slight non-linearity, attributed to redox reactions from pseudocapacitive effects, further confirming the synergistic contribution of EDLC and pseudo capacitance mechanisms.

The variations in specific capacitance with respect to current density are shown as Figure 6e. The capacitance of AC-TA-$Fe_{0.2}$ supercapacitor attains 61 $F \cdot g^{-1}$, which is notably greater than the 50 $F \cdot g^{-1}$ of the AC-based supercapacitor at 0.5 $A \cdot g^{-1}$, demonstrating the enhanced energy storage capacity achieved through TA and Fe modifications. Both devices show a reduction in capacitance with an increase in current density. However, at a high current density of 10 $A \cdot g^{-1}$, the AC-TA-$Fe_{0.2}$ supercapacitor retains a capacitance of 46 $F \cdot g^{-1}$, while the AC supercapacitor drops to approximately 36 $F \cdot g^{-1}$. This superior rate capability of AC-TA-$Fe_{0.2}$ is attributed to its pseudocapacitive mechanism and optimized pore structure, which enable more efficient charge transport and storage.

The cycling stability of the two supercapacitors at 5 $A \cdot g^{-1}$ over 10,000 times of charging and discharging is depicted (Figure 6f). Both exhibit excellent stability, with the AC-TA-$Fe_{0.2}$ supercapacitor maintaining a capacitance retention of nearly 97% and a constant coulombic efficiency above 98%. These results indicate that TA-Fe modifications not only enhance energy storage performance but also significantly improve the structural stability and resilience of the corresponding materials. Based on the specific capacitance and voltage window, the energy and power densities of assembled symmetric supercapacitors were calculated. The energy density achieved for AC-TA-$Fe_{0.2}$ based supercapacitor is 9.89 $Wh \cdot kg^{-1}$ at 550 $W \cdot kg^{-1}$ power density, and it still holds an energy density of 8.74 $Wh \cdot kg^{-1}$ at a power density of 2750 $W \cdot kg^{-1}$. In comparison, Zhang et al. [46] described a symmetric supercapacitor made from N/F-doped AC, achieving a specific capacitance of 26 $F \cdot g^{-1}$ at 1 $A \cdot g^{-1}$.

Likewise, Tolosa et al. [47] synthesized silicon oxycarbide-derived carbon fibers (SiOC), which demonstrated a specific capacitance of 135 $F \cdot g^{-1}$ at 10 $mV \cdot s^{-1}$ in a tetraethylammonium tetrafluoroborate/acetonitrile electrolyte, retaining 63% of its capacitance at high current densities. Arulepp et al. [48] developed TiC-derived carbon (TiC-CDC) electrodes with a specific capacitance of approximately 120 $F \cdot g^{-1}$ in organic electrolytes, corresponding to an energy density of around 10.8 $Wh \cdot L^{-1}$. In comparison, the AC-TA-Fe materials exhibit performance comparable to these studies. Moreover, the modification approach employed in our work is relatively simpler and can be readily adapted to various existing carbon-based substrates, such as carbon nanotubes and carbon fibers, offering high versatility and scalability.

4. Conclusion

This study developed AC-TA-Fe composites by coordinating TA with Fe^{3+}, greatly refining the structural and electrochemical properties of AC. The modification introduced redox-active sites, enhanced electrolyte accessibility, and optimized pore structure. Among the composites, AC-TA-$Fe_{0.2}$ achieved the best performance, having an energy density of 8.7 $Wh \cdot kg^{-1}$ at 2750 $W \cdot kg^{-1}$, maintaining close to 100% capacity after undergoing 10,000 cycles. The dynamic transition between pseudocapacitance and EDLC mechanisms emphasized its excellent rate performance. Moreover, this modification approach offers the advantages of using naturally abundant tannic acid and a straightforward synthesis process, potentially reducing production costs and environmental impact.

Acknowledgements

The authors gratefully acknowledge the supports from the Science and Technology Department of Henan Province (Grant No: 232102240005), China Scholarship Council (Grant No: 202208410248) and the Scientific Research Innovation Team of Xuchang University (Grant No: 2022CXTD006).

References

[1] Reenu, Sonia, L. Phor, A. Kumar, S. Chahal, Journal of Energy Storage 84 (2024) 110698. https://doi.org/10.1016/j.est.2024.110698

[2] Y.A. Kumar, N. Roy, T. Ramachandran, M. Hussien, M. Moniruzzaman, S.W. Joo, Journal of Energy Storage 98 (2024) 113040; https://doi.org/10.1016/j.est.2024.113040

[3] T. Li, S. Yang, Y. Zuo, W. Li, H. Yue, Š. Kment, Y. Chai, Inorganic Chemistry Frontiers 10 (2023) (3) 1001; https://doi.org/10.1039/D2QI01992B

[4] W. Li, T. Chen, A. Li, P. Shi, M. Wu, T. Li, H. Yue, Y. Chen, B. Huang, X. Lou, Inorganic Chemistry Frontiers 8 (2021) (4) 1093; https://doi.org/10.1039/D0QI01204A

[5] Y. Liu, B. Cheng, X. Xie, J. Chen, L. Wan, C. Du, Y. Zhang, M. Xie, Fuel 381 (2025) 133607; https://doi.org/10.1016/j.fuel.2024.133607

[6] T. Li, T. Jing, D. Rao, S. Mourdikoudis, Y. Zuo, M. Wang, Inorganic Chemistry Frontiers 9 (2022) (23) 6008; https://doi.org/10.1039/D2QI01911F

[7] M. Zhong, M. Zhang, X. Li, Carbon Energy 4 (2022) (5) 950; https://doi.org/10.1002/cey2.219

[8] Z. Zhai, L. Zhang, T. Du, B. Ren, Y. Xu, S. Wang, J. Miao, Z. Liu, Materials & Design 221 (2022) 111017; https://doi.org/10.1016/j.matdes.2022.111017

[9] R. Kumar, E. Joanni, S. Sahoo, J.-J. Shim, W.K. Tan, A. Matsuda, R.K. Singh, Carbon 193 (2022) 298; https://doi.org/10.1016/j.carbon.2022.03.023

[10] F. Wang, F. Zheng, J. Jiang, Y. Li, Y. Luo, K. Chen, J. Du, Y. Huang, Q. Li, H. Wang, Energy & Fuels 35 (2021) (9) 8334; https://doi.org/10.1021/acs.energyfuels.1c00337

[11] X.-h. Zhang, X.-y. Gan, B.-s. Liu, X.-y. Yan, X.-x. Zhao, New Carbon Materials 36 (2021) (3) 594; https://doi.org/10.1016/S1872-5805(21)60062-8

[12] X. Zhang, B. Liu, X. Yan, X. Zhao, Y. Zhang, Y. Wei, Q. Cao, Microporous and Mesoporous Materials 309 (2020) 110580; https://doi.org/10.1016/j.micromeso.2020.110580

[13] K.S. Lee, Y.J. Seo, H.T. Jeong, Carbon Letters 31 (2021) (5) 1041; https://doi.org/10.1007/s42823-020-00219-w

[14] Y. Deng, Y. Ji, H. Wu, F. Chen, Chem Commun (Camb) 55 (2019) (10) 1486; https://doi.org/10.1039/C8CC08391F

[15] N. Sahiner, Molecules 26 (2021) (9) 2429; https://doi.org/10.3390/molecules26092429

[16] Z. Guo, W. Xie, J. Lu, X. Guo, J. Xu, W. Xu, Y. Chi, N. Takuya, H. Wu, L. Zhao, Journal of Materials Chemistry B 9 (2021) (20) 4098; https://doi.org/10.1039/D1TB00383F

[17] J.Y. Oh, Y. Jung, Y.S. Cho, J. Choi, J.H. Youk, N. Fechler, S.J. Yang, C.R. Park, ChemSusChem 10 (2017) (8) 1675; https://doi.org/10.1002/cssc.201601615

[18] H. Ejima, J.J. Richardson, K. Liang, J.P. Best, M.P. van Koeverden, G.K. Such, J. Cui, F. Caruso, Science 341 (2013) (6142) 154; https://doi.org/10.1126/science.1237265

[19] Y. Wang, S. Chen, S. Zhao, Q. Chen, J. Zhang, Journal of Materials Chemistry A 8 (2020) (31) 15845; https://doi.org/10.1039/D0TA02229B

[20] Y. Lu, G. Zhang, H. Zhou, S. Cao, Y. Zhang, S. Wang, H. Pang, Angewandte Chemie 135 (2023) (41) e202311075; https://doi.org/10.1002/ange.202311075

[21] K. Ji, Y. Yue, P. Yang, Applied Surface Science 608 (2023) 155184; https://doi.org/10.1016/j.apsusc.2022.155184

[22] H. Wang, X. Li, Y. Jiang, M. Li, Q. Xiao, T. Zhao, S. Yang, C. Qi, P. Qiu, J. Yang, Angewandte Chemie 134 (2022) (14) e202200465; https://doi.org/10.1002/ange.202200465

[23] M. Liu, C. Cai, J. Li, J. Zhao, W. Teng, R. Liu, J Colloid Interface Sci 528 (2018) 1; https://doi.org/10.1016/j.jcis.2018.05.070

[24] R. Mehdi, S.R. Naqvi, A.H. Khoja, R. Hussain, Fuel 348 (2023) 128529; https://doi.org/10.1016/j.fuel.2023.128529

[25] S.K. Ramasahayam, U.B. Nasini, A.U. Shaikh, T. Viswanathan, J Power Sources 275 (2015) 835; https://doi.org/10.1016/j.jpowsour.2014.11.020

[26] Y. Deng, Y. Ji, H. Wu, F. Chen, Chemical Communications 55 (2019) (10) 1486; https://doi.org/10.1039/C8CC08391F

[27] J. Gao, Z.-Q. Wang, Z.-F. Wang, B. Li, Z.-Y. Liu, J.-J. Huang, Y.-T. Fang, C.-M. Chen, Journal of Colloid and Interface Science 658 (2024) 90; https://doi.org/10.1016/j.jcis.2023.12.037

[28] A. Janošević Ležaić, D. Bajuk-Bogdanović, J. Krstić, Z. Jovanović, Ž. Mravik, J. Kovač, N. Gavrilov, Fuel 312 (2022) 122930; https://doi.org/10.1016/j.fuel.2021.122930

[29] E.K. Kim, B.M. Lee, J.J. Park, J.H. Choi, J.M. Yun, Materials Today Sustainability 20 (2022) 100238; https://doi.org/10.1016/j.mtsust.2022.100238

[30] Z. Chen, Y. Chen, Q. Wang, T. Yang, Q. Luo, K. Gu, W. Yang, Journal of Colloid and Interface Science 665 (2024) 772; https://doi.org/10.1016/j.jcis.2024.03.177

[31] W. Liao, C. Yu, Z. Peng, F. Xu, Y. Zhang, W. Zhong, ACS Sustainable Chemistry & Engineering 11 (2023) (6) 2186; https://doi.org/10.1021/acssuschemeng.2c05386

[32] G. Zhou, Y. Ma, C. Gu, J. Yang, H. Pang, J. Li, L. Xu, Y. Tang, Inorganic Chemistry Frontiers 9 (2022) (6) 1091; https://doi.org/10.1039/D1QI01630J

[33] S.W. Bokhari, A.H. Siddique, P.C. Sherrell, X. Yue, K.M. Karumbaiah, S. Wei, A.V. Ellis, W. Gao, Energy Reports 6 (2020) 2768; https://doi.org/10.1016/j.egyr.2020.10.001

[34] F. Liu, S. Liao, H. Lin, Y. Yin, Y. Liu, H. Meng, Y. Min, ChemElectroChem 8 (2021) (14) 2686; https://doi.org/10.1002/celc.202100569

[35] P. Flouda, J. Yun, D. Loufakis, S.A. Shah, M.J. Green, D.C. Lagoudas, J.L. Lutkenhaus, Sustainable Energy & Fuels 4 (2020) (5) 2301; https://doi.org/10.1039/C9SE01299K

[36] F. Wu, F. Cui, Q. Ma, J. Zhang, X. Qi, T. Cui, Materials Letters 324 (2022) 132791; https://doi.org/10.1016/j.matlet.2022.132791

[37] W. Li, M. Wu, P. Shi, T. Li, H. Yue, Z. Dong, Y. Gao, X. Lou, Electrochim Acta 331 (2020) 135440; https://doi.org/10.1016/j.electacta.2019.135440

[38] H. Wang, J. Cao, Y. Zhou, Z. Wang, Y. Zhao, Y. Liu, H. Huang, M. Shao, Y. Liu, Z. Kang, Nanoscale 12 (2020) (34) 17925; https://doi.org/10.1039/D0NR05532H

[39] J. Castro-Gutiérrez, A. Celzard, V. Fierro, Frontiers in Materials 7 (2020); https://doi.org/10.3389/fmats.2020.00217

[40] T. Brezesinski, J. Wang, J. Polleux, B. Dunn, S.H. Tolbert, Journal of the American Chemical Society 131 (2009) (5) 1802; https://doi.org/10.1021/ja8057309

[41] J. Wang, J. Polleux, J. Lim, B. Dunn, The Journal of Physical Chemistry C 111 (2007) (40) 14925; https://doi.org/10.1021/jp074464w

[42] J. Zhang, H. Jiang, Y. Zeng, Y. Zhang, H. Guo, J Power Sources 439 (2019) 227026; https://doi.org/10.1016/j.jpowsour.2019.227026

[43] L. Wu, H. Li, X. Xie, K. Chai, P. Han, C. Zhang, C. Yang, Journal of Alloys and Compounds 780 (2019) 482; https://doi.org/10.1016/j.jallcom.2018.11.194

[44] S. Feng, D. Wang, W. Yang, J. Shen, Y. Zhu, S. Ni, Y. Zhou, M. Ye, S. Jiang, H. Dai, H. Xiao, J. Han, International Journal of Biological Macromolecules 285 (2025) 138381; https://doi.org/10.1016/j.ijbiomac.2024.138381

[45] T. Li, S. Yang, Y. Zuo, W. Li, H. Yue, Š. Kment, Y. Chai, Inorganic Chemistry Frontiers 10 (2023) (3) 1001; https://doi.org/10.1039/D2QI01992B

[46] J. Zhang, H. Yang, Z. Huang, H. Zhang, X. Lu, J. Yan, K. Cen, Z. Bo, Waste Disposal & Sustainable Energy 5 (2023) (3) 417; https://doi.org/10.1007/s42768-023-00155-1

[47] A. Tolosa, B. Krüner, N. Jäckel, M. Aslan, C. Vakifahmetoglu, V. Presser, J Power Sources 313 (2016) 178; https://doi.org/10.1016/j.jpowsour.2016.02.077

[48] M. Arulepp, J. Leis, M. Lätt, F. Miller, K. Rumma, E. Lust, A.F. Burke, J Power Sources 162 (2006) (2) 1460; https://doi.org/10.1016/j.jpowsour.2006.08.014